Ocean Sci. Discuss., 10, 1933–1969, 2013
www.ocean-sci-discuss.net/10/1933/2013/
doi:10.5194/osd-10-1933-2013

Ocean Science
Discussions
Open Access

Intrinsic variability of the Antarctic Circumpolar Current system: low- and high-frequency fluctuations of the Argentine Basin flow

G. Sgubin[1], S. Pierini[2], and H. A. Dijkstra[3]

[1]Laboratoire des Sciences du Climat et de l'Environnement, Paris, France
[2]Dipartimento di Scienze e Tecnologie, Università di Napoli Parthenope, Napoli, Italy
[3]Institute for Marine and Atmospheric research Utrecht, Utrecht University, the Netherlands

Received: 15 September 2013 – Accepted: 15 October 2013 – Published: 5 November 2013

Correspondence to: S. Pierini (stefano.pierini@uniparthenope.it)

Published by Copernicus Publications on behalf of the European Geosciences Union.

Abstract

In this paper, the variability of the Antarctic Circumpolar Current system produced by purely intrinsic nonlinear oceanic mechanisms is studied through a sigma-coordinate ocean model, implemented in a large portion of the Southern Ocean at an eddy-permitting resolution under steady surface heat and momentum fluxes. The mean transport through Drake Passage and the structure of the main Antarctic Circumpolar Current fronts are well reproduced by the model. Intrinsic variability is found to be particularly intense in the Subantarctic Front and in the Argentine Basin, on which further analysis is focused. The low-frequency variability at interannual time scales is related to bimodal behavior of the Zapiola Anticyclone, with transitions between a strong and collapsed anticyclonic circulation in substantial agreement with altimeter observations. Variability on smaller time scales shows clear evidence of topographic Rossby-mode propagation along the eastern and southern flanks of the Zapiola Rise and of mesoscale eddies, also in agreement with satellite altimeter observations. The analysis of the relationship between the low- and high-frequency variability suggests possible mechanisms of mutual interaction.

1 Introduction

Ocean model studies of various degrees of complexity forced by steady forcing have suggested in the last two decades that a substantial fraction of the low-frequency variability (LFV) of oceanic frontal structures (ranging from the interannual to the decadal and interdecadal time scales) may be due to highly nonlinear oceanic mechanisms internal to the ocean system: this is the so-called "intrinsic" LFV variability, that can advantageously be analyzed in the conceptual framework of dynamical systems theory (e.g., see Dijkstra, 2005; Dijkstra and Ghil, 2005, for reviews). The mechanisms can involve barotropic and baroclinic instability, eddy-mean flow interaction, Rossby wave propagation and interaction with topographic and coastal features. In general, identify-

OSD
10, 1933–1969, 2013

ing the intrinsic part of the ocean variability, and the modality through which it emerges, is necessary to assess the role played by the ocean in the global climate. In addition, studying these ocean changes is fundamental also from a modeling point of view, as they may not be properly represented even in high-resolution general circulation models due to their high sensitivity to the parameterization of unresolved processes. Most studies have been devoted to the major mid-latitude western boundary currents and of their extensions, such as the Kuroshio (e.g., Qiu and Miao, 2000; Schmeits and Dijkstra, 2001; Pierini, 2006, 2008; Pierini and Dijkstra, 2009; Pierini et al., 2009), the Gulf Stream (e.g., Schmeits and Dijkstra, 2001; Quattrocchi et al., 2012), and the Agulhas Current (e.g., Dijkstra and De Ruijter, 2001; Le Bars et al., 2012).

A good candidate for considerable intrinsic LFV is also the Antarctic Circumpolar Current (ACC) system (e.g., Rintoul et al., 2001) and its complex frontal structure in the Southern Ocean. The ACC plays an important role in the global climate through local water mass formation, ocean carbon sequestration and heat storage, and its means of connection of climate signals at all longitudes. Hogg and Blundell (2006) analyzed the LFV of the ACC by using an idealized multi-layer quasi-geostrophic model forced by steady winds. Their simulations display robust intrinsic LFV, which is shown to involve a positive feedback between baroclinic eddies and the mean circulation. Penduff et al. (2011) analyzed the sea level expression of intrinsic LFV in simulations of an eddy-permitting Ocean General Circulation Model (OGCM), and found their results in the Southern Ocean to be basically consistent with those of Hogg and Blundell (2006). O'Kane et al. (2013) used an OGCM (including sea ice) to identify a Southern Ocean southeast Pacific mode of intrinsic LFV through a suite of experiments that include low-frequency (ENSO, SAM) and high-frequency stochastic forcing. Giarolla and Matano (2013) used long time series of sea surface height (SSH), sea surface temperature and wind stress curl to determine the main modes of LFV of the Southern Ocean circulation, but they did not investigate its intrinsic component.

An oceanic region particularly relevant for climate that affects the Southern Ocean dynamics, and where important LFV was documented, is the Argentine Basin (AB),

OSD
10, 1933–1969, 2013

located in the South Atlantic sector near the South American coast. The AB is a crucial region where strongly contrasted water masses meet and mix (Fig. 1), and where the circulation is likely to influence meridional water exchanges between the Southern Ocean and subtropical latitudes (Piola and Gordon, 1989) with associated strong impact on the global climate system. An intense barotropic anticylonic circulation called Zapiola Anticyclone (ZA) was documented over the Zapiola Rise (ZR), a high sedimentary deposit located in the middle of the AB (Weatherly, 1993; Whitworth et al., 1991; Saunders and King, 1995). The ZA affects considerably the surface exchanges between the ACC and the South Atlantic Current (Smythe-Wright and Boswell, 1998) and is supposed to contribute to determine global deep water mass characteristics (Garzoli et al., 2008).

Significant LFV of the ZA was observed with in situ (Hughes, et al., 2007) and altimeter data (Saraceno et al., 2009). Saraceno et al. (2009) documented for the first time that the ZA flow may significantly decrease in strength or even vanish over an interannual time scale, with a cyclonic pattern emerging from time to time. Bigorre and Dewar (2009) developed an idealized quasi-geostrophic ocean process study about the circulation around a large scale topographic anomaly: the role of bottom friction and eddy diffusivity was found to be consistent with the theory proposed by Dewar (1998) for the mean flow, moreover the modeled LFV was shown to bear important similarities to that observed. Venaille et al. (2011) found intrinsic high- and low-frequency variability of the ZA in their comprehensive ocean model, and explained the internal part as the result of an eddy-driven stochastic process. In the same basin also high-frequency fluctuations were observed (Fu et al., 2001; Tai and Fu, 2005), and were interpreted in terms of topographic Rossby modes (Weijer et al., 2007a, b) and mesoscale variability (Fu, 2007).

In this paper, a model study aimed at identifying and analyzing the intrinsic variability of the ACC system, with a focus on its Subantarctic Front and relative effect on the AB flow, is presented. A primitive equation sigma-coordinate ocean model is implemented in a large portion of the Southern Ocean with an eddy-permitting resolution

OSD
10, 1933–1969, 2013

under steady forcing; the climatological forcing and the stratification are substantially idealized, while the topography (that plays a fundamental role at these high latitudes) is represented in more detail (Sect. 2). In Sect. 3 the LFV of the model flows is analyzed, with an emphasis on the AB where the highest level of variance is found. Regime switches occurring on interannual time scales of the AB flow are found to share important similarities with the long-term variations of the ZA as observed by Saraceno et al. (2009). In Sect. 4 the intrinsic high-frequency variability (HFV) in the AB, emerging as a residual from the LFV, is analyzed through a wavelet analysis and interpreted in terms of topographic Rossby modes and mesoscale eddies. In Sect. 5 the relation between the LFV and the HFV is analyzed by introducing dynamical indices, and possible mechanisms of mutual interaction are suggested. Finally, in Sect. 6 conclusions are drawn.

2 The model

The model used in this work (Sgubin, 2012) is the Princeton Ocean Model (POM) developed by Blumberg and Mellor in 1977 and subsequently improved and updated (for general information see www.aos.princeton.edu/WWWPUBLIC/htdocs.pom/). POM is a primitive equation sigma-coordinate model that contains a turbulence sub-model for vertical mixing based on the Mellor–Yamada scheme (Mellor and Yamada, 1982). Details of the model equations and numerical solution techniques can be found in the POM Users Guide (Mellor, 2003). The POM is a terrain-following model which yields realistic Ekman surface and bottom boundary layer flows: hence, it is particularly efficient in reproducing dynamic processes in the ACC because, due to the weak stratification and the important barotropic component, the dynamical balance is achieved mainly through the bottom form drag and topographic steering. The quantitative success of the ZA circulation model of de Miranda et al. (1999) was attributed to the use of this kind of vertical discretization (see also Barnier et al., 2006, for relevant modeling issues).

OSD
10, 1933–1969, 2013

The model domain includes Pacific and Atlantic sectors of the Southern Ocean, extending meridionally from 33.2° S to 72° S and longitudinally from 120° W to 0° W (Fig. 2). Periodic boundary conditions along the eastern and western meridional boundaries are imposed with a 12° transition region (with 10° to the west and 2° to the east; in that region the bathymetry is interpolated so as to match at the two boundaries). On the northern and southern boundaries free-slip boundary conditions are imposed at all depths. The Mercator projection is adopted with the ETOPO5 bathymetry data (available online at http://www.ngdc.noaa.gov/) on a grid with a horizontal spatial resolution of 1/5° in latitude and 1/2.5° in longitude. The Smagorinsky parameterization has been used for the horizontal eddy viscosity with the dimensionless HORCON parameter (Mellor, 2003) $H = 0.12$. The model has 12 vertical sigma levels and is integrated for 80 yr from motionless initial conditions with external and internal time steps $\Delta t_e = 20$ s and $\Delta t_i = 600$ s, respectively.

A drawback of sigma-coordinate models is the introduction of pressure gradient errors arising when computing the horizontal pressure gradient near very complex bathymetry (e.g., Beckmann and Haidvogel, 1993). This error is caused by large numerical truncations in the transformation from the z-coordinate to the sigma-coordinate. A reduction of such errors to acceptable values can be achieved by properly smoothing the bathymetry according to a criterion involving the bottom slope and the horizontal and vertical grid resolution, but, at the same time, such smoothing should retain the main features of the topography in order to consistently reproduce the interactions between the flow and the oceanic bottom, and should avoid hydrostatic inconsistency. This problem was successfully handled by Barnier et al. (1998), Marchesiello et al. (1998) and de Miranda et al. (1999) in setting up a consistent model for the South Atlantic circulation. We have therefore applied the method of Barnier et al. (1998) to obtain a topography (Fig. 2) that reduces drastically the pressure gradient error.

Following the approach typical of processes studies of the intrinsic LFV, an idealized but relatively realistic steady zonal wind stress field is used: Fig. 3a shows the wind stress profile based on the Trenberth et al. (1989) climatology. The imposed initial

OSD
10, 1933–1969, 2013

stratification, again idealized but relatively realistic, is shown in Fig. 3b for the temperature (the salinity has been held constant): it takes into account not only the vertical, but also the meridional density gradient which effectively influences the zonal flow at Drake Passage. In order to sustain such a stratification, an idealized steady surface heat flux has been imposed as well: this prevents the total mixing that would lead to vanishing meridional density gradient due to the vertical mixing provided by the POM.

Figure 4 shows the volume transport through the Drake Passage: the average value of ∼ 116 Sv is in reasonable agreement with the real estimated value of ∼ 130 Sv (e.g., Rintoul et al., 2001); an energetic HFV is present in the signal while the LFV in this integrated parameter is small. Fig. 5a and b show the mean SSH η and depth-integrated current $\mathbf{u}$, respectively: the position and structure of the main ACC fronts, i.e. the Polar Front and the Subantarctic Front, as well as the Malvinas Current are quite well captured by the model. The ZA has the correct shape and location, being centered at ∼ (315° E, 45° S). The Subtropical Front (located at around 39° S) associated with the Malvinas–Brazil Current Confluence is obviously absent due to the choice of the northern latitude of the domain of integration and of the wind forcing. However, this limitation does not affect our analysis, that is mainly focused on the intrinsic variability of the ZA directly induced by changes of the ACC frontal system, particularly through its Subantarctic Front. This is in fact an original aspect of the present study, in which these sources of intrinsic variability can be isolated.

3 Intrinsic low-frequency variability

In this section the LFV produced by the model is presented and discussed. The low-frequency signal has been derived by applying a moving average with $T = 200$ days at each grid point. The logarithm of the resulting rms of the SSH is shown in Fig. 6. Apart from a moderate variability in regions of strong topographic variations between ∼ 230–260° E and 345–360° E, a very intense LFV is present all along the Subantarctic

OSD
10, 1933–1969, 2013

Front between ∼302–345° E. The particularly intense variability across the southern topographic limits of the AB is consistent with the findings of Saraceno et al. (2009).

The analysis will therefore be focused on this region. Figure 7b shows the time series of the SSH taken in point P1 where the variability is maximum (see Fig. 7a), which is ∼2° south of the ZA center. The behavior is quite impressive, as it yields a chaotic vacillation of O(1 m) that has a bimodal character. A detailed analysis will be carried out within the 10 yr reference interval delimited by the red lines of Fig. 7b.

Figure 8 shows the SSH (total signal η: black line; low-frequency signal $\widetilde{\eta}$: blue line) in P1 during the reference interval; the SSH maps in the AB corresponding to the two sequences of six instants denoted by the green and red dots in Fig. 8 are shown in Fig. 9. In sequence (a) a well-defined ZA centered at (315° E, 46° S) is present at $t = 24\,600$ days, corresponding to a SSH maximum in P1, but one year before ($t = 24\,200$ days) and after ($t = 25\,000$ days) the anticyclonic circulation is weaker and shifted westward by 2–5°, while a cyclonic circulation moving from south-east intensifies and takes its place. Sequence (b) shows an abrupt transition from a collapsed but quite variable ZA ($t = 26\,200$–$26\,600$ days) to an intense ZA ($t = 27\,000$–$27\,200$ days). These transitions from a quasi-climatological ZA to a collapsed ZA (and vice-versa) are very similar to the variations of the ZA documented by Saraceno et al. (2009). The hypothesis is therefore that the oceanic intrinsic variability plays an important role in this phenomenon.

The preceding analysis has shown that a ZA in a quasi-climatological state is characterized by large values of $\widetilde{\eta}$ in P1 ($\widetilde{\eta} \approx 1$ m) while, for a collapsed ZA, $\widetilde{\eta} \approx 0$–$0.3$ m, thus Fig. 7b may provide qualitative information on the character and statistics of the transitions. However, $\widetilde{\eta}$ gives only very local information and is not necessarily indicative of a circulation regime. A better way to characterize the ZA state is to rely on the (dimensionless) relative vorticity ζ (and of its low-frequency version $\widetilde{\zeta}$) averaged over specific regions of the AB. The two maps of Fig. 10 show $\widetilde{\zeta}$ in a collapsed ($t = 25\,000$ days) and quasi-climatological state ($t = 27\,200$ days): it is evident that the two sectors A and B can very efficiently characterize the ZA state in terms of $\widetilde{\zeta}$ averaged in each of them.

OSD
10, 1933–1969, 2013

The graph of Fig. 10 shows $\langle\zeta\rangle_A$ (red line) and $\langle\zeta\rangle_B$ (blue line) as a function of time for the reference interval: as could be expected, in a collapsed state one has $\langle\zeta\rangle_A > 0$ and $\langle\zeta\rangle_B < 0$ whereas for a quasi-climatological state both parameters are positive, with a tendency of $\langle\zeta\rangle_B$ to be greater. Figure 11 shows the scatter plot of $\langle\widetilde{\zeta}\rangle_B$ vs. $\langle\widetilde{\zeta}\rangle_A$ for the whole 80 yr integration: the quasi-climatological state is represented by the compact cluster with $\langle\widetilde{\zeta}\rangle_B > 0$ while the collapsed state with $\langle\widetilde{\zeta}\rangle_B < 0$ is represented by a more diffuse cluster, which implies that this state cannot be characterized by a well defined circulation pattern, as is the case for the quasi-climatological state. Moreover, the abrupt character of the transitions is clearly shown by the small number of dots in the intermediate range. Possible mechanisms that govern this LFV will be discussed in Sect. 5.

4 Intrinsic high-frequency variability

In this section the high-frequency component of the intrinsic variability is analyzed, while its relation with the LFV will be considered in the next section. The high-frequency component is defined here in terms of the SSH as the residual $\eta' = \eta - \widetilde{\eta}$, and therefore includes periods lower than $T = 200$ days. Figure 12 shows the rms of η' in the AB: a region of intense variability crosses the isobaths from the deep sea just off the continental shelf in the south-west side of the ZR, reaching the peak of the ZR itself, and presents two maxima in P2 = (313° E, 47° S) and P3 = (317° E, 45.5° S). It is interesting to note that P3 corresponds almost exactly to the point P = (317° E, 45° S) in which a 25 day period counterclockwise-rotating dipole is centered, according to the altimeter observations of Fu et al. (2001) and Tai and Fu (2005).

The Figs. 13a and 14a show the time series of η' (red line) and $\widetilde{\eta}$ (blue line). The HFV has a very intermittent behavior and yields an apparent relation with the LFV in that the high frequency is more energetic when the low frequency is in a collapsed state, corresponding to low values of $\widetilde{\eta}$. Because of the intermittency of the HFV (also found in altimeter data by Tai and Fu, 2005, and Fu, 2007), a spectral analysis can most appro-

OSD
10, 1933–1969, 2013

priately be carried out by means of the continuous wavelet transform (e.g., Torrence and Compo, 1998). The Figs. 13b and 14b show the amplitude $w(s,t)$ of the wavelet transform of η in points P2 and P3, respectively (only the time scales $s \leq 200$ days are shown). In the period band $s = 0$–50 days, which includes topographic Rossby waves and modes (Fu et al., 2001), the amplitude is reduced and very intermittent over time scales ranging from 100 to 300 days (in agreement with Fu, 2007). In the period band $s = 100$–150 days the amplitude is higher and less intermittent, but is often clearly related to the higher frequency variability (this also is consistent with the results of Fu, 2007, but see the next section for a more careful comparison).

For a qualitative analysis of the flow patterns of the HFV, sequences of snapshots of the SSH residual η' are reported in the Figs. 15 and 16. In Fig. 15 two 25 day long sequences sampled every 5 days are shown corresponding to two maxima in the wavelet amplitude in P2 in the period band $s = 0$–50 days, and analogously for Fig. 16 but for point P3. Very complex patterns arise, with length scales ranging from O(1°) or less for the mesoscale up to O(5°–10°) for the topographic Rossby modes observed by Fu et al. (2001). The variability is mainly confined over the ZR and shows a clear propagation of features originating from the south-western side of the ZR; such wave trains follow the southern limits of the ZR and turn counterclockwise along the eastern side of the topographic rise. For instance, in sequence (a) of Fig. 15 there is initially ($t = 24\,380$ days) a wave train with three highs and three lows traveling eastward following the isobaths, but eventually the vortices rotate counterclockwise being trapped over the ZR, and in doing so they undergo substantial stretching and deformation. In sequence (b) of both Figs. 15 and 16 the rotation is even more evident. These waves can be interpreted as topographic Rossby modes that, as we have already pointed out, are well known to occur over the ZR (Fu et al., 2001; Tai and Fu, 2005; Weijer et al., 2007a, b). The patterns appear more complex than those typically shown in this location by altimeter data after high-pass filtering the motions with time scales longer than ~ 1 month (e.g., Fu et al., 2001). This is because our high-frequency signal contains also the longer-term variability associated with the mesoscale eddy field.

OSD
10, 1933–1969, 2013

A general feature that deserves to be emphasized is the varying length scale of the vortices, that is smaller in the south-west side of the ZR and tends to increase as the pattern propagates. This transition from the mesoscale to the Rossby mode scale is compatible with the energy exchange found to be at work in this region by Fu (2007): this aspect will be analyzed in more detail in the next section. From this qualitative analysis it appears that the topographic Rossby modes in the ZR are not necessarily generated resonantly by the wind forcing but also intrinsically. Presumably this happens through lower frequency fluctuations of the local circulation (Pierini, 1996; Pierini et al., 2002), that in this case are intrinsic. This also supports the hypothesis that the wind generated topographic Rossby modes may as well be generated through the same mechanism, in which case the current fluctuations that produce them are not intrinsic but directly wind-driven.

5 Relation between low- and high-frequency variability

In the Sects. 3 and 4 we have identified intrinsic LFV on interannual time scales yielding regime switches from a quasi-climatological ZA to a collapsed ZA, but HFV was found as well. A high-frequency range (s = 0–50 days) includes topographic Rossby modes; an intermediate high-frequency range (s = 100–150 days) appears to be related to the first frequency range. Now, a question arises: is there a relation between these three forms of intrinsic variability in our model results? In general, analyzing this issue is fundamental from a theoretical viewpoint, as it could shed light into dynamical mechanisms that involve a wide range of spatial and temporal scales in a unique region in this respect, such as the AB.

A preliminary qualitative analysis of this kind is presented here. First of all we define a Zapiola index as follows:

$$Z = \langle\widetilde{\zeta}\rangle_{\mathrm{A}} - \langle\widetilde{\zeta}\rangle_{\mathrm{B}} \quad (1)$$

OSD
10, 1933–1969, 2013

The graph of Fig. 10 shows $\langle\zeta\rangle_A$ and $\langle\zeta\rangle_B$ for the reference interval: the two signals are virtually in counterphase in a ZA collapsed state while they tend to be both positive in a quasi-climatological ZA state, with the second signal being higher. Thus, Z as defined in Eq. (1) (and shown by the green line in Fig. 17 for the reference interval) is a good global low-frequency indicator of the ZA state, for which a large positive value implies a collapsed state, while a negative or small positive value implies a quasi-climatological state. To construct high-frequency indices we can define the integral of the wavelet amplitude in P3 (the most representative point for the HFV in the AB) within two time scales:

$$W_{s_1,s_2}(t) = \int_{s_1}^{s_2} w_{P_3}(s,t)\mathrm{d}s \quad (2)$$

Thus, the two indices $W_{0,50}$ and $W_{100,150}$ (red and blue lines of Fig. 17, respectively) are good indicators of the behavior in the two high-frequency ranges, as explained below. We pass to discuss three possible interactions suggested by Fig. 17 and by other experimental and numerical investigations.

5.1 Relation between $W_{100,150}$ and Z

Several works (e.g., Dewar, 1998; Bigorre, 2005; Bigorre and Dewar, 2009; Volkov and Fu, 2008; Venaille et al., 2011) have suggested that the mesoscale eddy activity provides the man source of energy of the ZA. By studying the correlation between the eddy kinetic energy and the LFV of the ZA with 15 yr of altimeter records, Saraceno et al. (2009) found support of that hypothesis, suggesting a rapid adjustment of the ZA to changes in the eddy kinetic energy. By using high-resolution altimeter data produced by the Archiving, Validation and Interpretation of Satellite Oceanographic data (AVISO) project, Fu (2007) found that the variance-preserving spectrum of the mesoscale energy time series in the AB is spread over a wide range of frequencies, with the majority in the seasonal-to-interannual range, but a significant variance is present also in the

OSD
10, 1933–1969, 2013

high-frequency range corresponding to periods of 100–160 days. Thus $W_{100,150}$ represents a good index for the HFV related to the mesoscale in the AB. In our model results, both transitions present in the reference interval from a collapsed to a quasi-climatological ZA (occurring at $t \approx 24\,400$, 26 700 days when Z decreases abruptly, Fig. 17) are preceded by a large $W_{100,150}$, which decreases as the transition to the quasi-climatological state is occurring, with a lag of 100–300 days between the two signals. Moreover, the collapse of the ZA at $t \approx 24\,700$ days is followed by an increase of $W_{100,150}$ with a lag of $\sim$200 days. This behavior is compatible with a transfer of energy from the eddy field to the large scale circulation during the collapsed ZA – quasi-climatological ZA transition, and vice-versa, and therefore seems to be in basic agreement with the theoretical and experimental arguments reported above: it is interesting to note that purely intrinsic oceanic mechanisms are able to produce such dynamical process.

5.2 Relation between $W_{0,50}$ and $W_{100,150}$

Using altimeter observations, Fu (2007) analyzed the possible relationship between the 25 day barotropic Rossby waves and the energetic baroclinic mesoscale eddies in the ZA region. The wave amplitude was found to be coherent with the energy of the high-frequency mesoscale variability, in that when the latter decreases the wave amplitude increases and vice-versa, suggesting an exchange of energy between the two scales. A clear sign of this behavior in our model results (for which changes in the wave amplitude and in the mesoscale eddy field are represented by $W_{0,50}$ and $W_{100,150}$, respectively) can be found in the intervals $t \approx 23\,800$–$24\,700$ days and $t \approx 25\,900$–$26\,400$ days (Fig. 17), which both precede the transition from a collapsed to a quasi-climatological ZA state. The latter property is particularly interesting, as it suggests a relationship between the energy exchange in the high-frequency range and the large-scale LFV of the ZA that deserves to be analyzed in future studies.

OSD
10, 1933–1969, 2013

5.3 Relation between $W_{0,50}$ and Z

During the transition from a quasi-climatological to a collapsed ZA in the interval $t \approx 24\,600$–$25\,000$ days no relationship such as the one described above seems to exist between $W_{0,50}$ and $W_{100,150}$; on the other hand, the sudden increase of the energy level in $W_{0,50}$ follows the abrupt collapse of the ZA. This suggests that an impulsive generation of topographic Rossby modes can be active, perhaps with the involvement of mesoscale eddies as discussed at the end of Sect. 4. To this respect, laboratory experiments in a rotating tank performed by Pierini et al. (2002) confirmed the hypothesis put forward in a previous numerical study on topographic Rossby modes in the Strait of Sicily (Pierini, 1996), according to which topographic Rossby modes can effectively be excited by rapid changes of the mean flow (provided in the tank by the movement of a large paddle). In a Rossby mode the time scale is set by the bottom topography and coastlines (if present) and not by the spectral content of the wind field, which only indirectly forces the modes through changes in the mean flow. This may explain why Fu et al. (2001) did not find any significant wind variability at periods close to 25 days in the AB, nor could they find any significant correlation between the variability of the wave amplitude and the variability of the wind stress curl. Thus, the impulsive generation of topographic Rossby modes, which appears to be active in our numerical results, should be considered when explaining the HFV in the temporal range $s = 0$–50 days.

It is clear that understanding the intricate mutual interaction among these three different temporal scales requires a much deeper investigation than that presented in this analysis, which cannot by itself determine any causality between the various scales. Nonetheless, these results can complement those quoted above for future, more advanced investigations in this very peculiar and interesting oceanic site.

OSD
10, 1933–1969, 2013

6 Conclusions

In this paper, an eddy-permitting sigma-coordinate ocean model has been applied to a large portion of the Southern Ocean with the aim of identifying and analyzing low- and high-frequency fluctuations of intrinsic oceanic origin – a fundamental task for understanding the role of the ocean in the global climate. The approach is typical of process-oriented studies of the intrinsic oceanic variability (idealized but relatively realistic steady winds and stratification), but a realistic topography is used because barotropic motions, and so topographic interactions, are important here. The obtained mean flow is in good agreement with observations as far as the transport through the Drake Passage and the structure of the main Antarctic Circumpolar Current fronts are concerned. Important variability of both low- and high-frequency nature is found, being particularly intense in the branch of the Subantarctic Front corresponding to the Argentine Basin, which, due to its crucial location plays an active role in determining the circulation in the south-west Atlantic sector of the Southern Ocean. The variability over interannual time scales shows a bimodal behavior of the Zapiola Anticyclone, connecting a quasi-climatological state to a state in which the anticyclonic circulation collapses and sometimes reverses locally: this is in substantial agreement with the altimeter observations of Saraceno et al. (2009). The high-frequency residual signal shows clear evidence of mesoscale propagating patterns particularly along the southern flanks of the Zapiola Rise, and a counterclockwise rotation of larger scale topographic Rossby modes over the rise, in substantial agreement with observations. Thus, the main conclusion is that these forms of variability are compatible with intrinsic generation mechanisms all internal to the ocean system. A preliminary analysis of the mutual relationship between the low-frequency variability and two components of the high-frequency variability yields behaviors that are consistent with observations and previous theoretical and modeling studies, and at the same time suggests a deeper analysis of the results.

Future perspectives include studies devoted to analyze the sensitivity of the model response to changes in the forcing and parameterizations. For example, changing the

OSD
10, 1933–1969, 2013

amplitude of the wind forcing and/or the parameterization of dissipative effects could produce important modifications in the intrinsic variability (e.g., see the analysis of Pierini et al., 2009, in the context of the Kuroshio Extension bimodality). Another fundamental aspect that should be analyzed is the effect of time-dependent forcing on the emergence of the intrinsic oceanic variability. The intrinsic variability is often in the form of relaxation oscillations that are self-sustained beyond a given tipping point (global bifurcation in some state space) associated with a particular control parameter, while they do not emerge below that threshold under steady forcing (e.g., Simonnet et al., 2005). However, if an appropriate noise or deterministic time-dependent component is added to the forcing, the same intrinsic relaxation oscillations can emerge even below the bifurcation point (e.g., Pierini, 2010, 2011; 2012). Thus, using steady forcing constitutes only the first step toward the identification of the intrinsic variability: further studies that include both wind noise and the main modes of atmospheric variability in the Southern Ocean will have to be carried out.

Acknowledgements. This research was supported by the MATH-ACC Project funded by the Italian "Programma Nazionale di Ricerche in Antartide" (PNRA Contract n. 2010/A2.11-2753). The work of HD was also sponsored by the COMPLEXITY Project PreKurs funded by the "Netherlands Organization for Scientific Research" (NWO).

References

Barnier, B., Marchesiello, P., de Miranda, A. P., Molines, J.-M., and Coulibaly, M.: A sigma-coordinate primitive equation model for studying the circulation in the South Atlantic. Part I: Model configuration with error estimates, Deep-Sea Res., 45, 543–572, 1998.

Barnier, B. and collaborators: Impact of partial steps and momentum advection schemes in a global ocean circulation model at eddy permitting resolution, Ocean Dynam., 56, 543–567, 2006.

Beckmann, A. and Haidvogel, D.: Numerical simulation of flow around a tall isolated seamount. Part I: Problem formulation and model accuracy, J. Phys. Oceanogr., 23, 1736–1753, 1993.

OSD
10, 1933–1969, 2013

Bigorre, S.: Topographic effects on wind driven oceanic circulation, Ph. D. Thesis, Florida State University, 100 pp., 2005.
Bigorre, S. and Dewar, W. K.: Oceanic time variability near a large scale topographic circulation, Ocean Model., 29, 176–188, 2009.
De Miranda, A. P., Barnier, B., and Dewar, W. K.: On the dynamics of the Zapiola Anticyclone, J. Geophys. Res., 104, 21139–21149, 1999.
Dewar, W. K.: Topography and barotropic transport control by bottom friction, J. Mar. Res., 56, 295–328, 1998.
Dijkstra, H. A.: Nonlinear Physical Oceanography, Springer, 532 pp., 2005.
Dijkstra, H. A. and de Ruijter, W. P. M.: On the physics of the Agulhas Current: steady retroflection regimes, J. Phys. Oceanogr., 31, 2971–2985, 2001.
Dijkstra, H. A. and Ghil, M.: Low-frequency variability of the large-scale ocean circulation: a dinamical systems approach, Rev. Geophys., 43, RG3002, doi:10.1029/2002RG000122, 2005.
Fu, L.-L.: Interaction of mesoscale variability with large-scale waves in the Argentine Basin, J. Phys. Oceanogr., 37, 787–793, 2007.
Fu, L.-L., Cheng, B., and Qiu, B.: 25-day period large-scale oscillations in the Argentine Basin revealed by the TOPEX/Poseidon altimeter, J. Phys. Oceanogr., 31, 506–517, 2001.
Garzoli, S. L., Piola, A. R., Speich, S., Baringer, M., Goni, G., Donohue, K., Meinen, C., and Matano, R. P.: A monitoring system for heat and mass transports in the South Atlantic as a component of the meridional overturning circulation, Workshop Report: Estancia San Ceferino, Buenos Aires, Argentina, 8–10 May 2007, International CLIVAR Project Office, Southampton, UK, 38 pp., 2008.
Giarolla, E. and Matano, R. P.: The low-frequency variability of the Southern Ocean circulation, J. Climate, 26, 6081–6091, 2013
Hogg, A. M. and Blundell, J. R.: Interdecadal variability of the Southern Ocean, J. Phys. Oceanogr., 36, 1626–1645, 2006.
Hughes, C. W., Stepanov, V. N., Fu, L.-L., Barnier, B., and Hargreaves, G. W.: Three forms of variability in Argentine Basin ocean bottom pressure, J. Geophys. Res., 112, C01011, doi:10.1029/2006JC003679, 2007.
Le Bars, D., de Ruijter, W. P. M., and Dijkstra, H. A.: A new regime of the Agulhas Current retroflection: turbulent choking of Indian-Atlantic leakage, J. Phys. Oceanogr., 42, 1158–1172, 2012.

OSD
10, 1933–1969, 2013

Marchesiello, P., Barnier, B., and de Miranda, A. P.: A sigma-coordinate primitive equation model for studying the circulation in the South Atlantic. Part II: Meridional transport and seasonal variability, Deep-Sea Res., 45, 573–608, 1998.
Mellor, G. L.: Users Guide for a Three-Dimensional, Primitive Equation, Numerical Ocean Model, Prog. in Atmos., and Ocean Sci., Princeton University, 53 pp., 2003.
Mellor, G. L. and Yamada, T.: Development of a turbulence closure model for geophysical fluid problems, Rev. Geophys., 20, 851–875, 1982.
O'Kane, T. J., Matear, R. J., Chamberlain, M. A., Risbey, J. S., Sloyan, B. M., and Horenko, I.: Decadal variability in an OGCM Southern Ocean: intrinsic modes, forced modes and metastable states, Ocean Model., 69, 1–21, 2013.
Penduff, T., Juza, M., Barnier, B., Zica, J., Dewar, W. K., Treguier, A.-M., Molines, J.-M., and Audiffren, N.: Sea level expression of intrinsic and forced ocean variabilities at interannual time scales, J. Climate, 24, 5652–5670, 2011.
Pierini, S.: Topographic Rossby modes in the strait of sicily, J. Geophys. Res., 101, 6429–6440, 1996.
Pierini, S.: A Kuroshio Extension system model study: decadal chaotic self-sustained oscillations, J. Phys. Oceanogr., 36, 1605–1625, 2006.
Pierini, S.: On the crucial role of basin geometry in double-gyre models of the Kuroshio Extension, J. Phys. Oceanogr., 38, 1327–1333, 2008.
Pierini, S.: Coherence resonance in a double-gyre model of the Kuroshio Extension, J. Phys. Oceanogr., 40, 238–248, 2010.
Pierini, S.: Low-frequency variability, coherence resonance and phase selection in a low-order model of the wind-driven ocean circulation, J. Phys. Oceanogr., 41, 1585–1604, 2011.
Pierini, S.: Stochastic tipping points in climate dynamics, Phys. Rev. E, 85, 027101, doi:10.1103/PhysRevE.85.027101, 2012.
Pierini, S. and Dijkstra, H. A.: Low-frequency variability of the Kuroshio Extension, Nonlinear Proc. Geoph., 16, 665–675, 2009.
Pierini, S., Fincham, A., Renouard, D., D'Ambrosio, R., and Didelle, H.: Laboratory modeling of topographic Rossby normal modes, Dynam. Atmos. Oceans, 35, 205–225, 2002.
Pierini, S., Dijkstra, H. A., and Riccio, A.: A nonlinear theory of the Kuroshio Extension bimodality, J. Phys. Oceanogr., 39, 2212–2229, 2009.
Piola, A. R. and Gordon, A. L.: Intermediate waters in the southwest South Atlantic, Deep-Sea Res., 36, 1–16, 1989.

OSD
10, 1933–1969, 2013

Qiu, B. and Miao, W.: Kuroshio path variations south of Japan: bimodality as a self-sustained internal oscillation, J. Phys. Oceanogr., 30, 2124–2137, 2000.
Quattrocchi, G., Pierini, S., and Dijkstra, H. A.: Intrinsic low-frequency variability of the Gulf Stream, Nonlinear Proc. Geoph., 19, 155–164, 2012.
Rintoul, S. R., Hughes, C., and Olbers, D.: The Antarctic Circumpolar Current system, in: Ocean Circulation and Climate, Academic Press, 271–302, 2001.
Saraceno, M., Provost, C., and Zajaczkovski, U.: Long-term variation in the anticyclonic ocean circulation over the Zapiola Rise as observed by satellite altimetry: evidence of possible collapses, Deep-Sea Res., 56, 1077–1092, 2009.
Saunders, P. and King, B. A.: Bottom currents derived from a shipborne ADCP on WOCE cruise A11 in the South Atlantic, J. Phys. Oceanogr., 25, 329–347, 1995.
Schmeits, M. J. and Dijkstra, H. A.: Bimodal behavior of the Kuroshio and the Gulf Stream, J. Phys. Oceanogr., 31, 3435–3456, 2001.
Sgubin, G.: A model study of the Southern Ocean dynamics: mean flow, intrinsic variability and teleconnections, Ph. D. Thesis, University of Naples "Federico II" and University of Naples "Parthenope", 130 pp., 2012.
Simonnet, E., Ghil, M., and Dijkstra, H. A.: Quasi-homoclinic behavior of the barotropic quasi-geostrophic double-gyre circulation, J. Mar. Res., 63, 931–956, 2005.
Smythe-Wright, D. and Boswell, S.: Abyssal circulation in the Argentine Basin, J. Geophys. Res., 103, 15845–15851, 1998.
Tai, C.-K. and Fu, L.-L.: 25-day period large-scale oscillations in the Argentine Basin revisited, J. Phys. Oceanogr., 35, 1473–1479, 2005.
Torrence, C. and Compo, G. P.: A practical guide to wavelet analysis, B. Am. Meteorol. Soc., 79, 61–78, 1998.
Trenberth, K. E., Olson, J. G., and Large, W. G.: A global ocean wind stress climatology based on ECMWF analyses, NCAR Technical Note NCAR/TN-338, 1989.
Venaille, A., Le Sommer, J., Molines, J.-M., and Barnier, B.: Stochastic variability of oceanic flows above topography anomalies, Geophys. Res. Lett., 38, L16611, doi:10.1029/2011GL048401, 2011.
Volkov, D. L. and Fu, L.-L.: The role of vorticity fluxes in the dynamics of the Zapiola Anticyclone, J. Geophys. Res., 113, C11015, doi:10.1029/2008JC004841, 2008.
Weatherly, G. L.: On deep-current and hydrographic observations from a mudwave region and elsewhere in the Argentine Basin, Deep-Sea Res., 40, 939–961, 1993.

OSD
10, 1933–1969, 2013

Weijer, W., Vivier, F., Gille, S. T., and Dijkstra, H. A.: Multiple oscillatory modes of the Argentine Basin. Part I: Statistical analysis, J. Phys. Oceanogr., 37, 2855–2868, 2007a.

Weijer, W., Vivier, F., Gille, S. T., and Dijkstra, H. A.: Multiple oscillatory modes of the Argentine Basin. Part II: The spectral origin of basin modes, J. Phys. Oceanogr., 37, 2869–2881, 2007b.

Whitworth, T., Nowlin, W. D., Pillsbury, R. D., Moore, M. I., and Weiss, R. F.: Observations of the Antarctic Circumpolar Current and deep boundary current in the southwest Atlantic, J. Geophys. Res., 96, 15105–15118, 1991.

OSD
10, 1933–1969, 2013

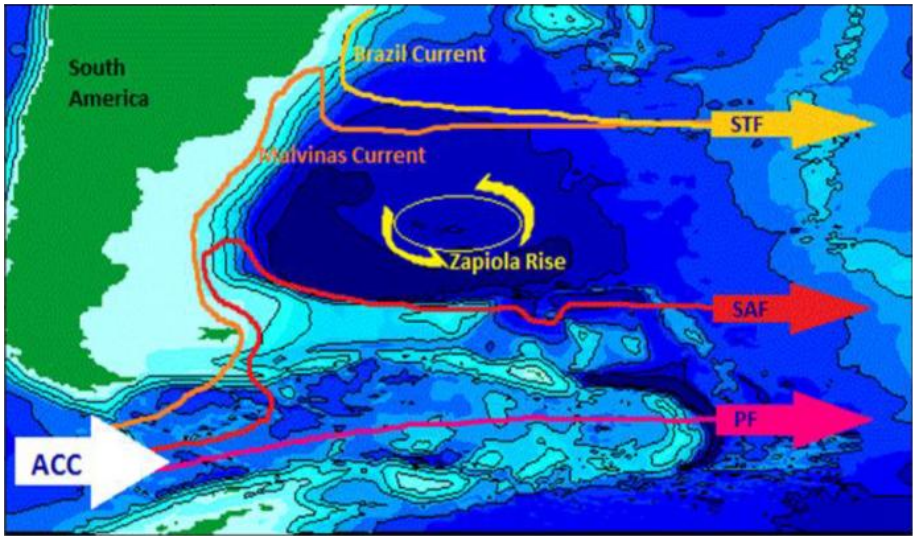

Fig. 1. Sketch of the circulation in the western South Atlantic. The ACC dominates the southern part of the basin, splitting into two major fronts, the Polar Front and the Subantarctic Front. Part of this water turns north forming the Malvinas current. From the North, the Brazil Current flows southward along the continental shelf, colliding with the Malvinas Current at around 39° S, where it creates the very energetic and turbulent region known as the Malvinas–Brazil Current Confluence.

OSD
10, 1933–1969, 2013

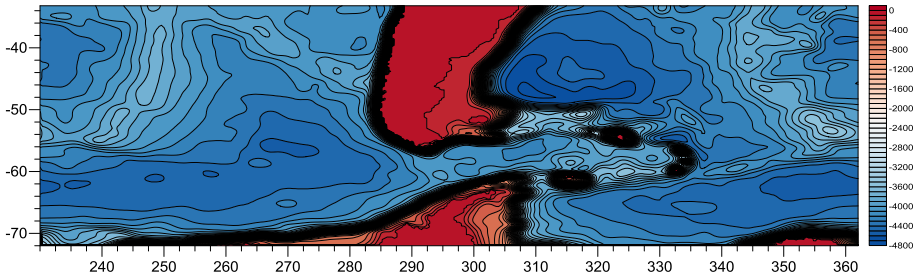

Fig. 2. Domain of integration and bottom topography.

OSD
10, 1933–1969, 2013

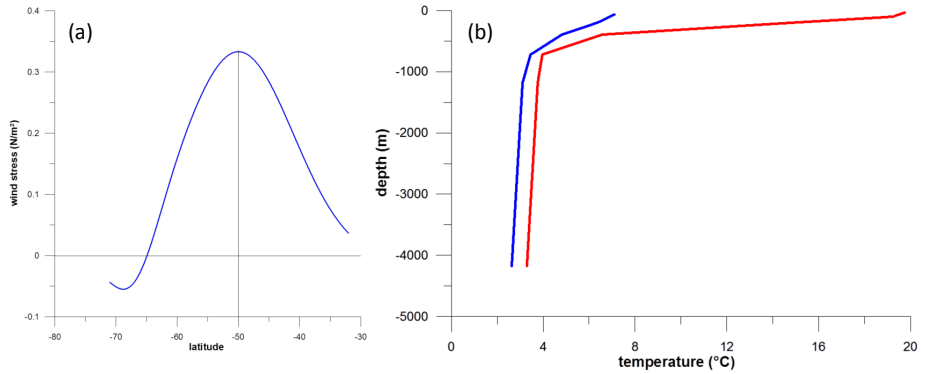

Fig. 3. (a) Steady zonal wind stress profile used to force the circulation model. **(b)** Initial stratifications (red/blue line: temperature profile at the northernmost/southernmost latitude).

OSD
10, 1933–1969, 2013

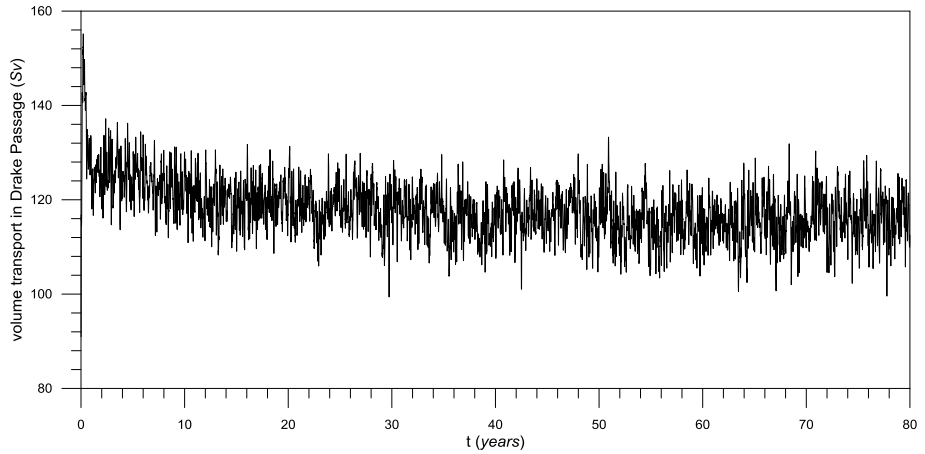

Fig. 4. Volume transport across the Drake Passage.

OSD
10, 1933–1969, 2013

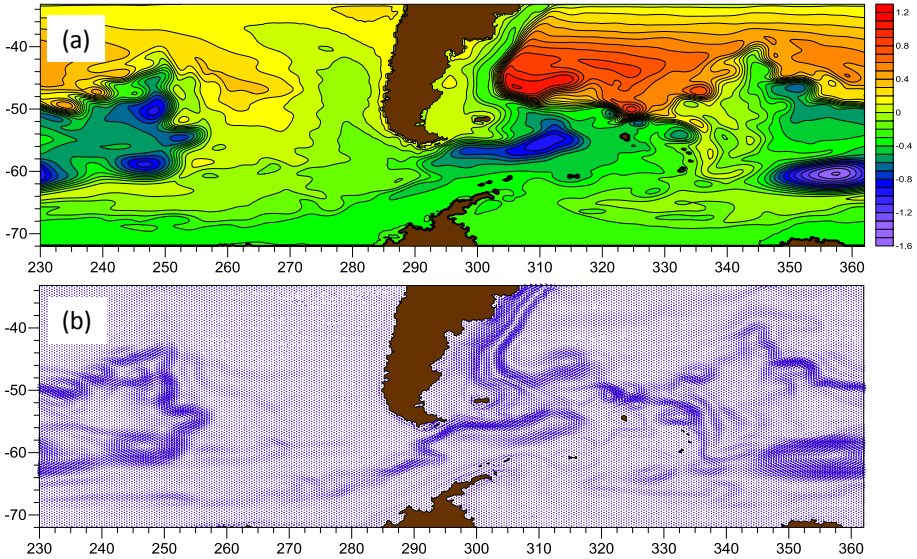

Fig. 5. (a) Mean SSH (in m). **(b)** Mean depth-integrated currents.

OSD
10, 1933–1969, 2013

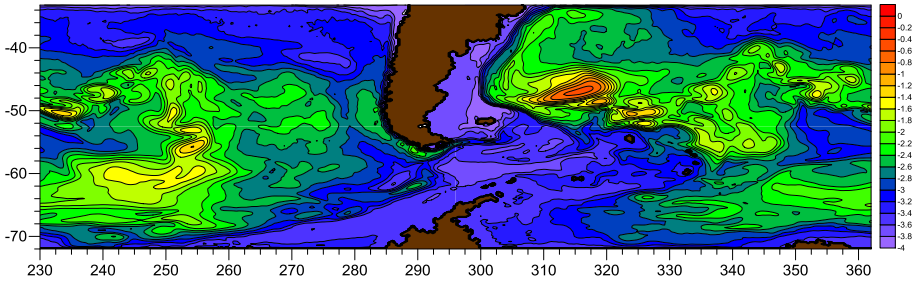

Fig. 6. Logarithm of the rms of the low-frequency SSH signal.

OSD
10, 1933–1969, 2013

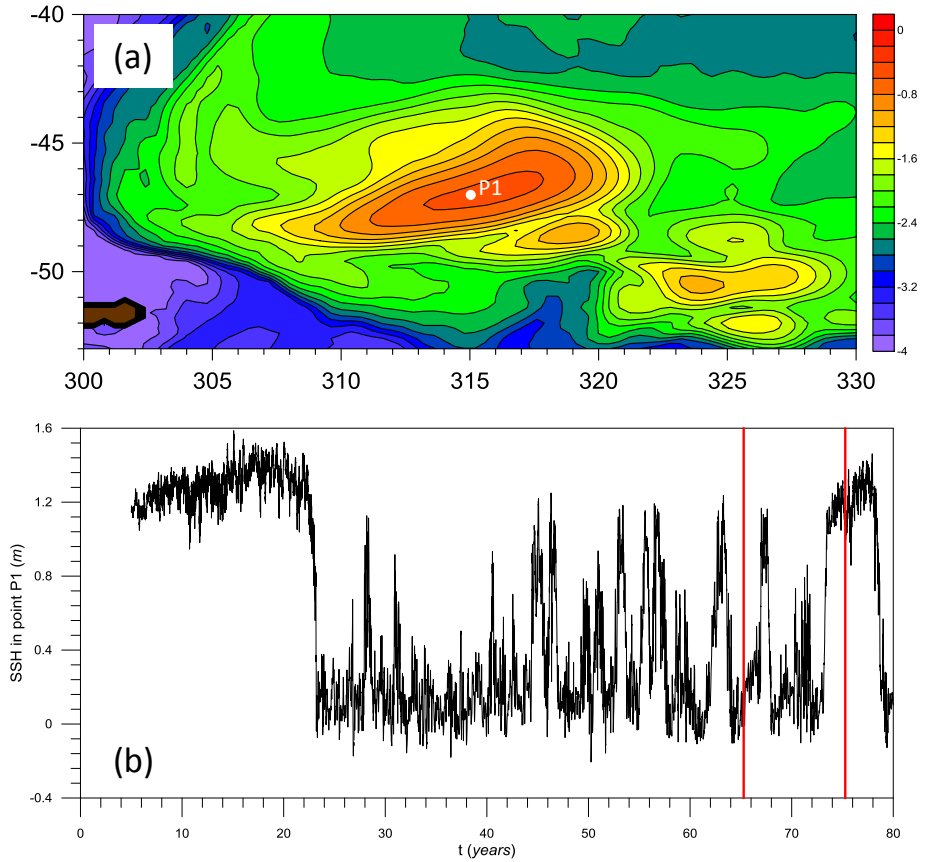

Fig. 7. (a) Logarithm of the rms of the low-frequency SSH signal in the Argentine Basin. **(b)** SSH in P1 (the analyses are carried out within the 10 yr reference interval delimited by the red lines).

OSD
10, 1933–1969, 2013

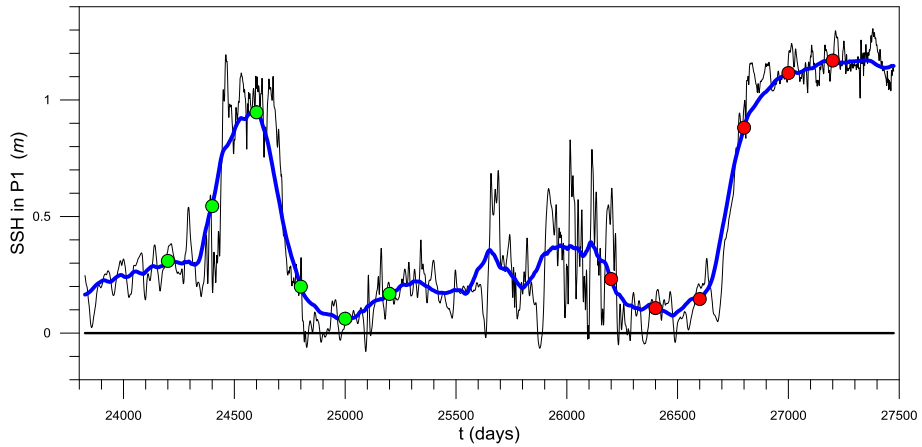

Fig. 8. SSH in P1 for the reference interval (black line: total signal; blue line: low-frequency signal). The SSH snapshots corresponding to the green/red dots are shown in Fig. 9.

OSD
10, 1933–1969, 2013

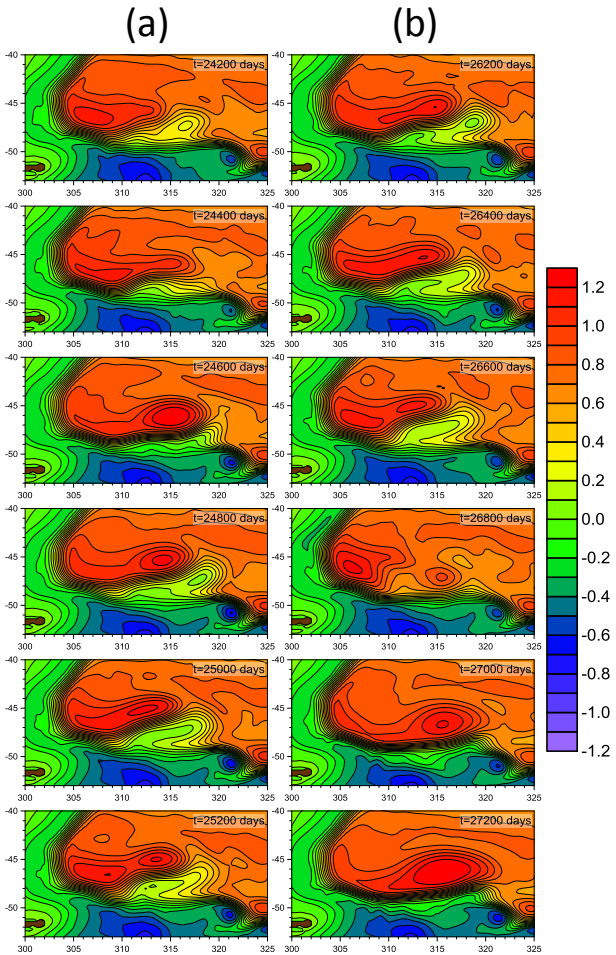

Fig. 9. Snapshots of the low-frequency SSH signal (in m) corresponding to the green (column **a**) and red (column **b**) dots of Fig. 8.

OSD
10, 1933–1969, 2013

Intrinsic variability of the Antarctic Circumpolar Current

G. Sgubin et al.

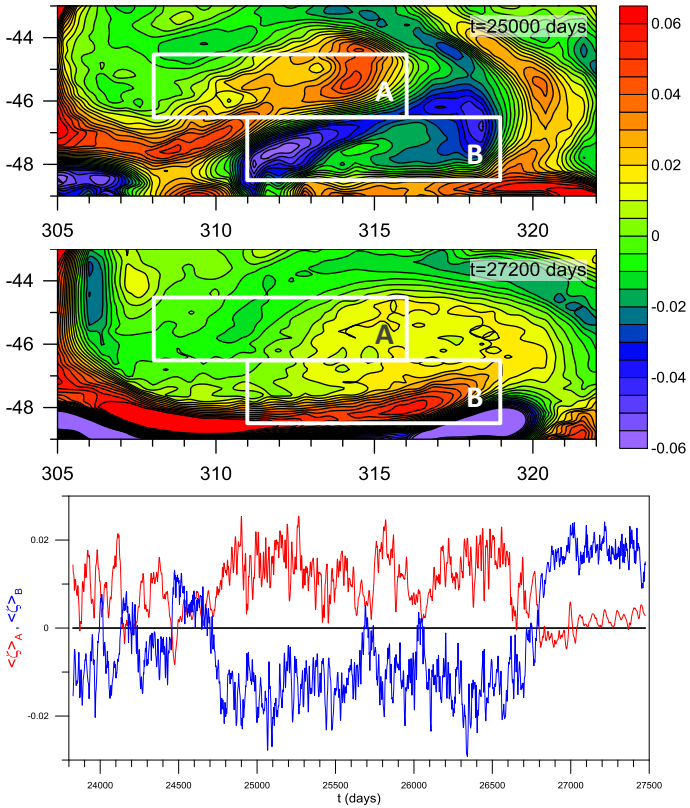

Fig. 10. Upper panels: low-frequency relative vorticity $\tilde{\zeta}$ at t = 25 000, 27 200 days. Lower panel: time series of ζ averaged in sectors A and B for the 10 yr reference interval.

OSD
10, 1933–1969, 2013

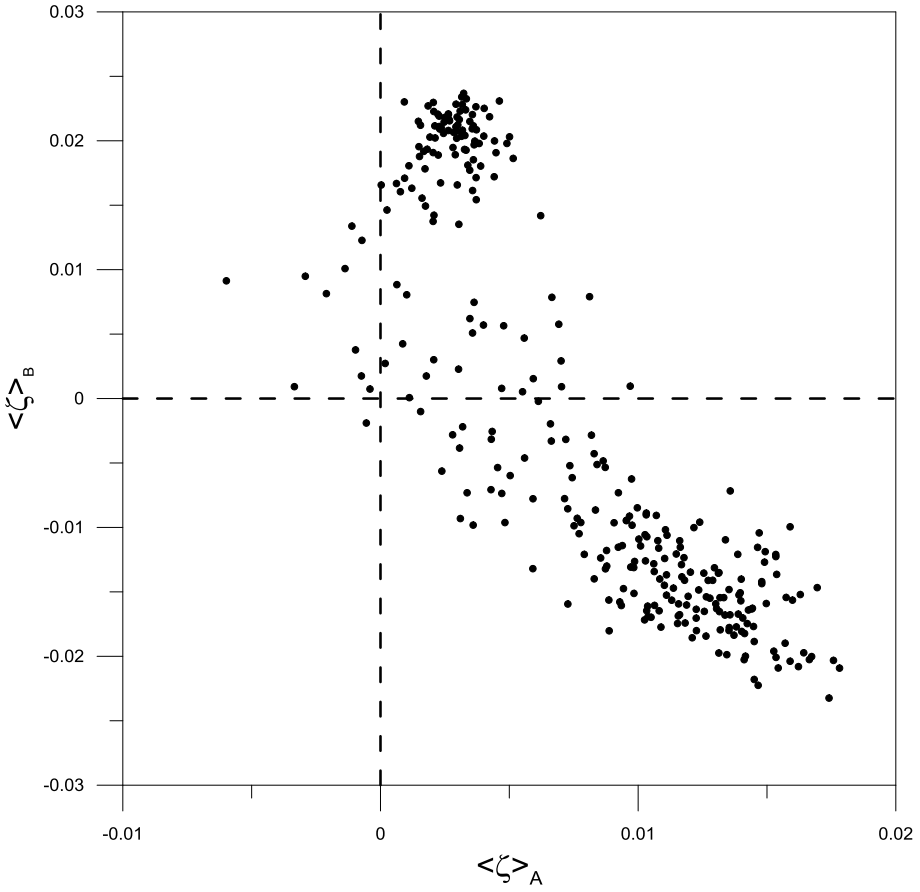

Fig. 11. Scatter plot of $\widetilde{\zeta}$ averaged in sectors A and B.

OSD
10, 1933–1969, 2013

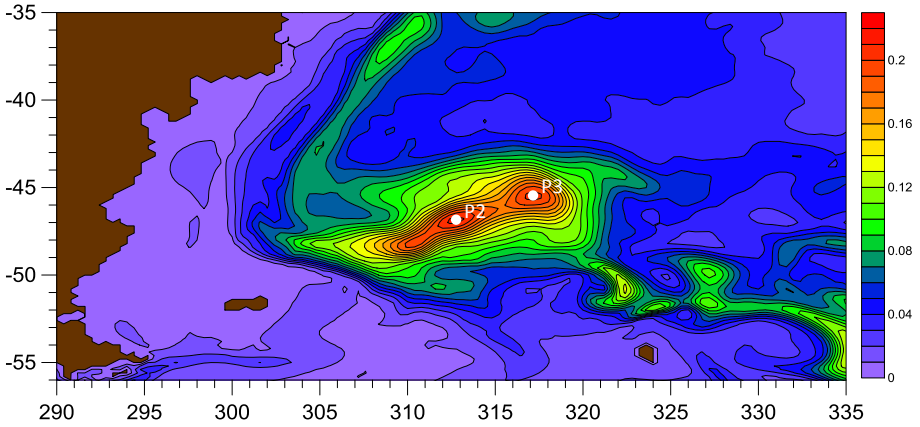

Fig. 12. Rms of the high-frequency SSH signal (in m) in the Argentine Basin.

OSD
10, 1933–1969, 2013

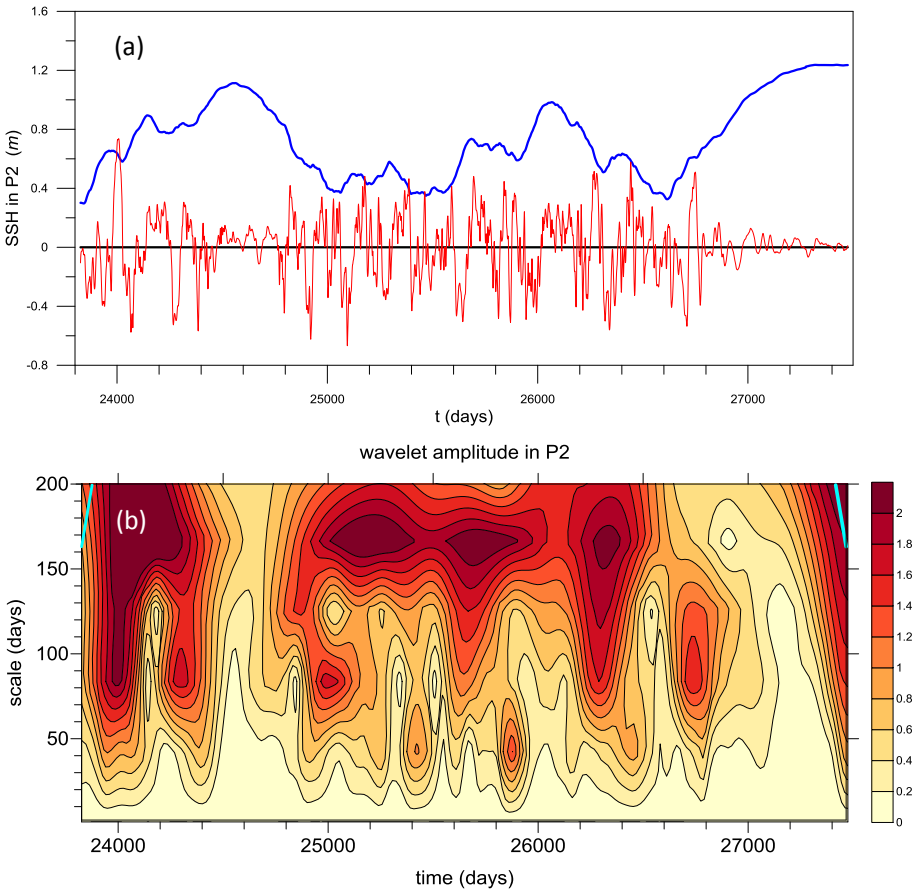

Fig. 13. (a) Low-frequency SSH in P2 (blue line) and corresponding high-frequency residual (red line). **(b)** Wavelet amplitude of the SSH signal in P2 for the reference interval (the cyan lines indicate the cone of influence).

OSD
10, 1933–1969, 2013

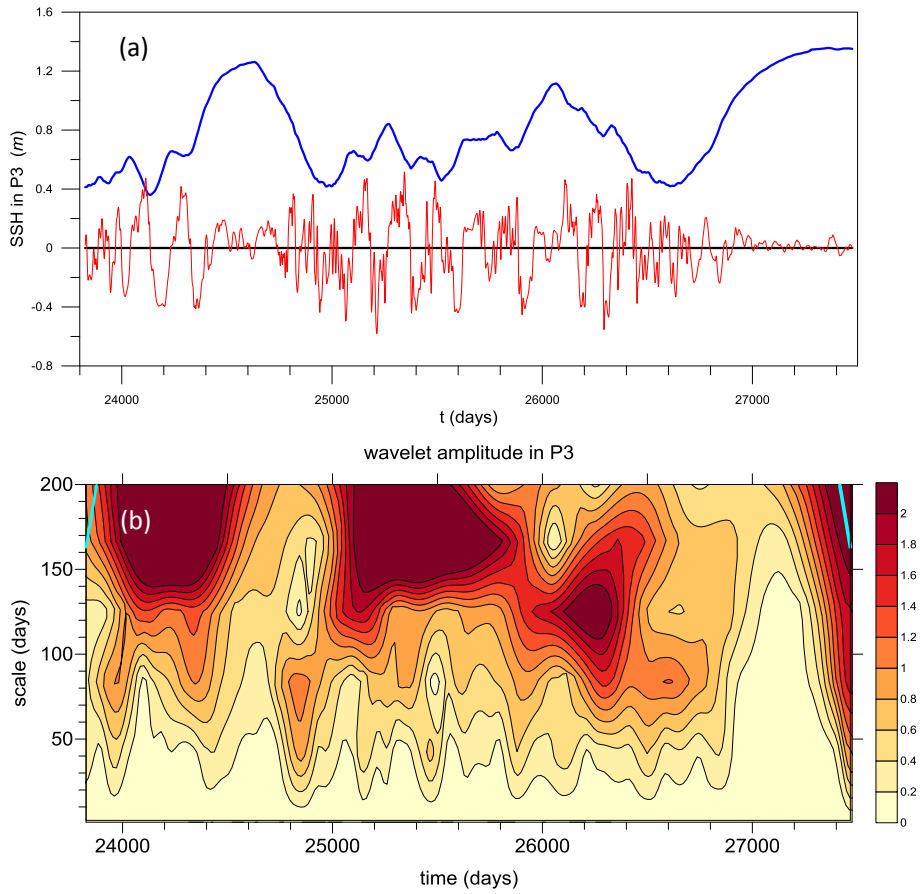

Fig. 14. As in Fig. 13 but for point P3.

OSD
10, 1933–1969, 2013

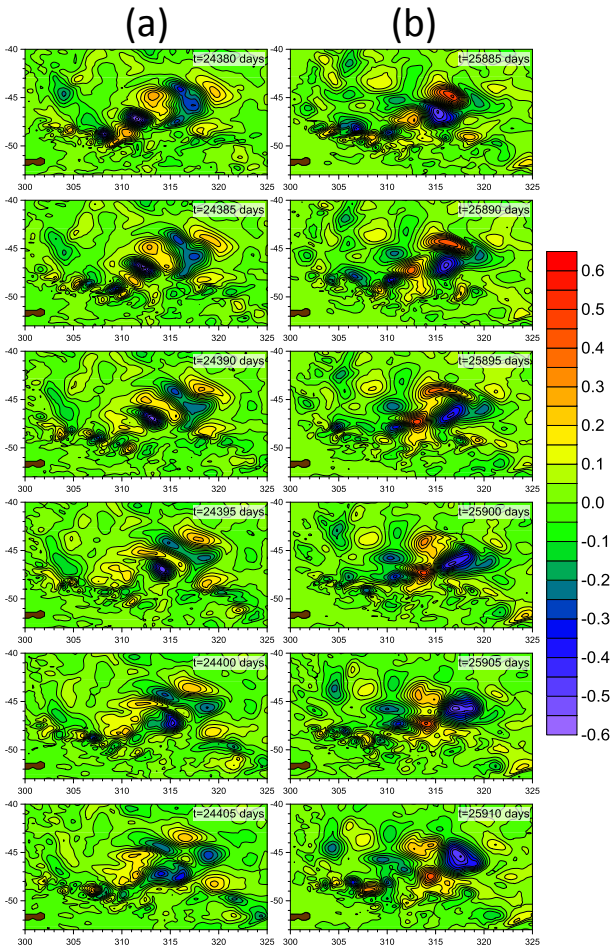

Fig. 15. Snapshot sequences **(a, b)** of the SSH high-frequency residual (in m) corresponding to two high-frequency maxima of the wavelet amplitude in P2.

OSD
10, 1933–1969, 2013

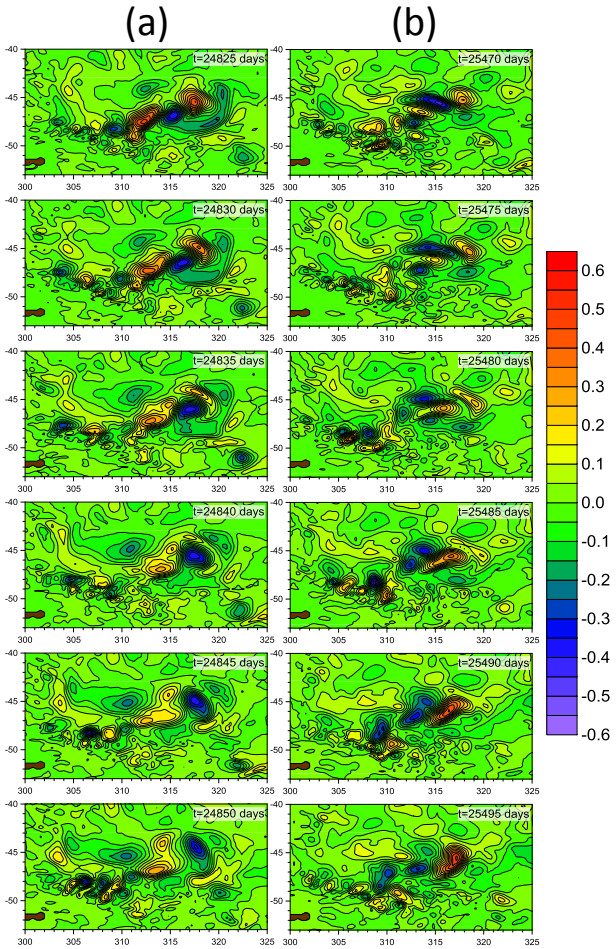

Fig. 16. Snapshot sequences **(a, b)** of the SSH high-frequency residual (in m) corresponding to two high-frequency maxima of the wavelet amplitude in P3.

OSD
10, 1933–1969, 2013

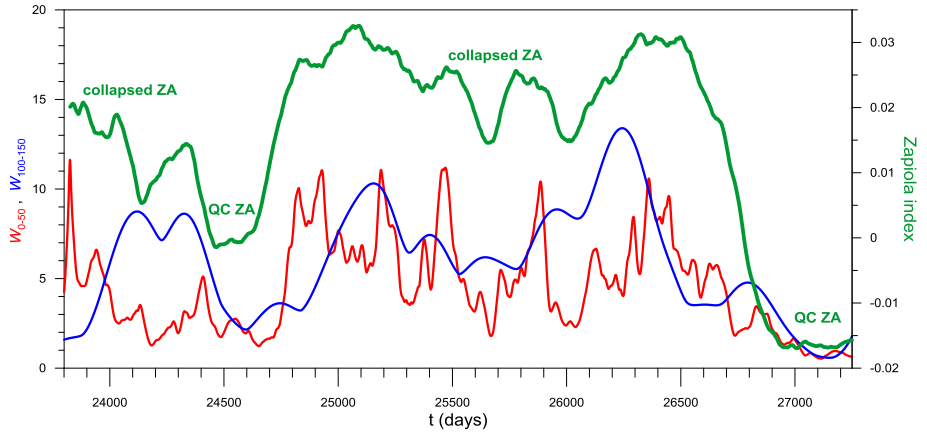

Fig. 17. Green line: zapiola index. Red and blue lines: integrated wavelet amplitudes $W_{0,50}$ and $W_{100,150}$, respectively.

OSD
10, 1933–1969, 2013